

Distinct Recrystallization Kinetics in Ni–Co–Cr–Fe-Based Single-Phase High-Entropy Alloys



ZHONGSHENG YANG, FENG HE, QINGFENG WU, KAIWEI ZHANG, DINGCONG CUI, BOJING GUO, BIN HAN, JUNJIE LI, JINCHENG WANG, and ZHIJUN WANG

Recrystallization has been a major method to induce heterogeneous grain structure for improving the strength–ductility combination of single-phase high-entropy alloys (HEAs). However, the recrystallization kinetics, which are the guideline for controlling the recrystallization behavior, of single-phase HEAs are relatively less explored. Here, we uncover the recrystallization behaviors of typical single-phase NiCoCrFe and Ni₂CoCrFe HEAs. Our results showed that the two investigated HEAs exhibit almost similar recrystallization activation energy around 230 kJ·mol⁻¹, but distinctively different recrystallization kinetics. This abnormal difference is attributed to the deformation twins of NiCoCrFe. These findings indicate that, except for textbook factors, deformation twinning significantly enhances the recrystallization behavior of HEAs.

<https://doi.org/10.1007/s11661-021-06341-2>

© The Minerals, Metals & Materials Society and ASM International 2021

I. INTRODUCTION

HIGH-ENTROPY alloys (HEAs) show great potential in breaking the property limits of metals and provide a flexible model to accelerate the development of physical metallurgy.^[1,2] Recently, heterogeneous grain structure (HGS) has shown a great chance in balancing the strength and ductility of metals and alloys.^[3–5] This efficient strengthening approach has also been applied to enhance the mechanical properties of HEAs.^[6,7] Broadly speaking, multiscale-grain HEAs,^[8–10] eutectics HEAs,^[11–13] and precipitation-hardened HEAs^[14–17] can also be viewed as HGS HEAs. Such combinations of HGS strengthening strategy and multiprincipal alloys design concept have achieved remarkable properties,

opening an effective way to overcome strength–ductility trade-off.^[18–21]

Meanwhile, it is widely recognized that the HGS can be obtained by partial recrystallization, which is the handiest and most economical thermal–mechanical processing (TMP).^[5] Recrystallization refers to the transformation of a metastable deformation state to a stable recrystallization state.^[22] However, the reported TMP processes to get partially recrystallized samples are inefficient. It relies on a time-consuming trial-and-error approach, especially in the choice of annealing temperature and time. For example, HGS with 39 pct recrystallized fraction and 76 pct recrystallized fraction were obtained when annealed at 600 for 1 and 4 hours, respectively, in the single-phase NiCoCr HEA with 70 pct reduction in thickness.^[9] Similar HGS microstructure was also obtained in Al_{0.1}CoCrFeNi at 600 °C for 1 hour of annealing.^[23] A full recrystallization microstructure can be obtained in NiCoCr by annealing for 1 hour at temperatures higher than 700 °C.^[9] These works showed that annealing temperature and time significantly influenced the recrystallization volume, but related quantified study describing the relationship among these three parameters is still limited. In addition, HGS was retained in Ti and Al doped NiCoCr HEA when annealed at 900 °C for 1 hour, indicating that the addition of Ti and Al changed the recrystallization kinetics.^[8] The higher recrystallization temperature caused by the addition of Ti and Al was also found in NiCoCrFeMn HEA.^[24] It is, therefore, obvious

ZHONGSHENG YANG, QINGFENG WU, KAIWEI ZHANG, DINGCONG CUI, BOJING GUO, JUNJIE LI, JINCHENG WANG, and ZHIJUN WANG are with the State Key Laboratory of Solidification Processing, Northwestern Polytechnical University, Xi'an 710072, People's Republic of China. Contact e-mail: zhjwang@nwpu.edu.cn FENG HE is with the State Key Laboratory of Solidification Processing, Northwestern Polytechnical University, and also with Centre for Advanced Nuclear Safety and Sustainable Development, City University of Hong Kong, Hong Kong, People's Republic of China. Contact e-mail: fenghe@mail.nwpu.edu.cn BIN HAN is with the Institute of Atomic and Molecular Science, Shaanxi University of Science and Technology, Xi'an 710021, Shaanxi, People's Republic of China.

Manuscript submitted February 2, 2021; accepted May 23, 2021.

that the recrystallized kinetics varied with the chemical compositions of HEAs. However, the origin of this composition dependence is still not fully understood. In light of the above two points, the quantified study on recrystallization kinetics of HEAs becomes the prerequisite for precisely adjusting of HGS.

As for the recrystallization kinetics of HEAs, Annasamy *et al.*^[25,26] reported that NiCoCrFeAl_x exhibited a decreased rate of recrystallization comparing with traditional alloys because of a high activation energy (549 kJ·mol⁻¹). This high activation energy was attributed to the distorted lattice, sluggish diffusion, and the interaction between Al–Ni rich precipitates and recrystallization. A low activation energy of ~ 232.7 kJ·mol⁻¹ was obtained in single-phase HEA NiCoCrFeN_{0.7}.^[27] It was again attributed to the sluggish diffusion effect of HEAs. However, the sluggish diffusion effect has been debated in recent years.^[28–30] On the other hand, stacking fault energy has been suggested to play a role in the recrystallization of HEAs. For example, the recrystallization kinetics of Fe₅₀Mn₃₀Co₁₀Cr₁₀ were enhanced by the reverse transformation of strain-induced martensite. Meanwhile, an even lower recrystallization activation energy of 108 kJ·mol⁻¹ was obtained for this HEA. The authors argued that the low stacking fault energy (SFE) of the Fe₅₀Mn₃₀Co₁₀Cr₁₀ HEA led to the phase transformation and thus low recrystallization activation energy.^[31] In addition, Wu *et al.*^[32] also reported that SFE could profoundly affect the recrystallization kinetics of HEAs. Despite these pioneering works, two important issues concerning the recrystallization of HEAs remain unclear. Firstly, the recrystallization kinetics of single-phase HEAs, which are the most used systems in obtaining HGS, are still limited. Secondly, how SFE affects the recrystallization behavior of HEAs is still confusing.

Therefore, we in the current study investigated the static recrystallization behaviors of two single-phase HEAs of NiCoCrFe and Ni₂CoCrFe with different SFE^[33–35] using the metallographic method. The recrystallization kinetics of the two HEAs were analyzed using the Arrhenius equation and Johnson–Mehl–Avrami–Kolmogorov (JMAK) model which applies to describe the kinetics of materials.^[36] Scanning electron microscope (SEM), electron backscattered diffraction (EBSD), transition electron microscope (TEM) were used to characterize deformed microstructures and to uncover the effect of SFE on the recrystallization kinetics of single-phase HEAs.

II. EXPERIMENTS

Samples of NiCoCrFe and Ni₂CoCrFe were produced by arc melting pure (> 99.5 pct) constituent metals under an argon atmosphere in which Ti getter was employed to prevent potential oxygen contamination and then casted into a copper mold with the dimension of 50 mm × 10 mm × 5 mm. Each sample was remelted for four times to promote the chemical homogeneity. Ingots were further homogenized for 2 hours at 1200 °C followed by water quenching. After homogenized treatment, HEAs were

cold-rolled to ~ 1.5 mm (~ 70 pct thickness reduction). The recrystallization heat treatment was carried out at 575, 600, and 650 °C from 5 to 300 minutes unequally and quenched in water to keep the recrystallized microstructure. Selection of the annealing temperature was based on the empirical recrystallization temperature ~ 0.6 T_m (melting point), which was an appropriate temperature to study the recrystallization kinetics and ensure the fully recrystallization within an acceptable and controllable annealing time (the melting point was calculated by the JMatPro with the Nickel-based Superalloy database in Figure 8). Considering the requirement of annealing time and accuracy of experiment, 575 °C and 650 °C were also chosen to study the recrystallization kinetics since the activation energy can be obtained from the Arrhenius equation of different temperatures. Selection of the annealing time was random from 5 to 300 minutes and interval of annealing time became larger with time increasing.

The X-ray diffraction (XRD) patterns of the homogenized, cold-rolled and annealed samples were obtained by Rigaku d/max-2550 with monochromator. The SEM samples were initially grinded to 2500-grit SiC paper, then electron-polished in a solution of perchloric acid and alcohol (50:450 mL) with a direct voltage of 30 V for 8–10 seconds at ambient temperature, and finally analyzed by SEM (Tescan MIRA3) equipped with back scattered electron (BSE) and EBSD detectors (Oxford Instruments). The method described in Reference [37] was adopted here to obtain recrystallized fraction and the average value of three images with view field of 800 μm was used as one data point. TEM (JEOL 2100F) was used to identify the deformation microstructures under 200 kV. A twin-jet polishing technique was used to prepare the TEM specimens. Sheet samples with the thickness of 0.5 mm were first cut from the center of the samples by electrical discharged machining (EDM) and then mechanically ground to a thickness of ~ 50 μm using SiC papers. Then the samples were punched into 3-mm-diameter disks and further thinned in a mixture of a 10 pct volume percent perchloric acid and 90 pct alcohol at – 30 °C with 50 V. The dog-bone specimens with gauge dimension of 12.5 × 1.2 × 3 mm³ were prepared for the tensile test with a strain rate of 1 × 10⁻³ s⁻¹ at ambient temperature.

III. RESULTS AND DISCUSSION

XRD patterns of the initial and annealed microstructures of NiCoCrFe and Ni₂CoCrFe are presented in Figure 1. NiCoCrFe is denoted as A and Ni₂CoCrFe is denoted as B; meanwhile H, CR and PRX are used to represent homogenized state, cold-rolled state, partially recrystallized state. PRX samples, NiCoCrFe and Ni₂CoCrFe are annealed for 53 and 61 minutes under 600 °C, respectively. From the characteristic peaks, fcc structure can be clearly identified, indicating that all the microstructures of homogenized, cold-rolled, and partially recrystallized states are single-phase fcc structure.

The representative images for different stages of the recrystallization process, *i.e.*, the begin of recrystallization (< 10 pct), low recrystallization fraction (10–30

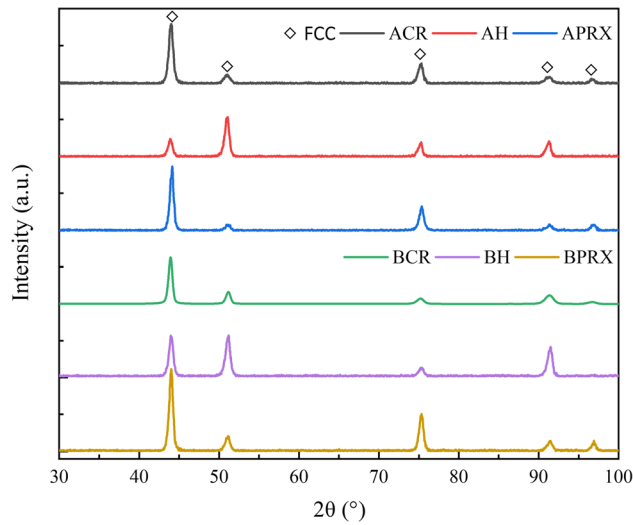


Fig. 1—XRD patterns of NiCoCrFe and Ni₂CoCrFe under cold-rolled, homogenized and partially recrystallized states.

pct), high recrystallization fraction (50–70 pct), and almost full recrystallization (> 90 pct) are shown in Figures 2 and 3. Figure 2 shows the representative partially recrystallized microstructures of NiCoCrFe. As shown in Figure 2(a), deformed NiCoCrFe starts to recrystallize after 11 minutes annealing at 600 °C. The recrystallized grains are featured by clear boundary and uniform contrast under BSE mode. The fraction of recrystallized area increases as the annealing time increases (Figures 2(b) and (c)). The microstructure of NiCoCrFe after annealed for 75 minutes at 600 °C in Figure 2(d) shows that recrystallized fraction reaches up to 95 pct. A similar microstructure evolution is observed in Ni₂CoCrFe (Figures 3(a) through (d)). The quantified recrystallized fractions as a function of annealing time at different temperatures are presented in Figure 4, and the representative microstructures used for measuring the recrystallized volume fractions can be seen in Electronic Supplementary Figures S1, S2, S3, S4, S5, S6, S7, S8, S9, S10, S11, S12, S13, S14, S15, S16, S17, S18, S19, S20, S21, S22, S23, S24, S25, and S26. It is intriguing that the two HEAs show significant difference in

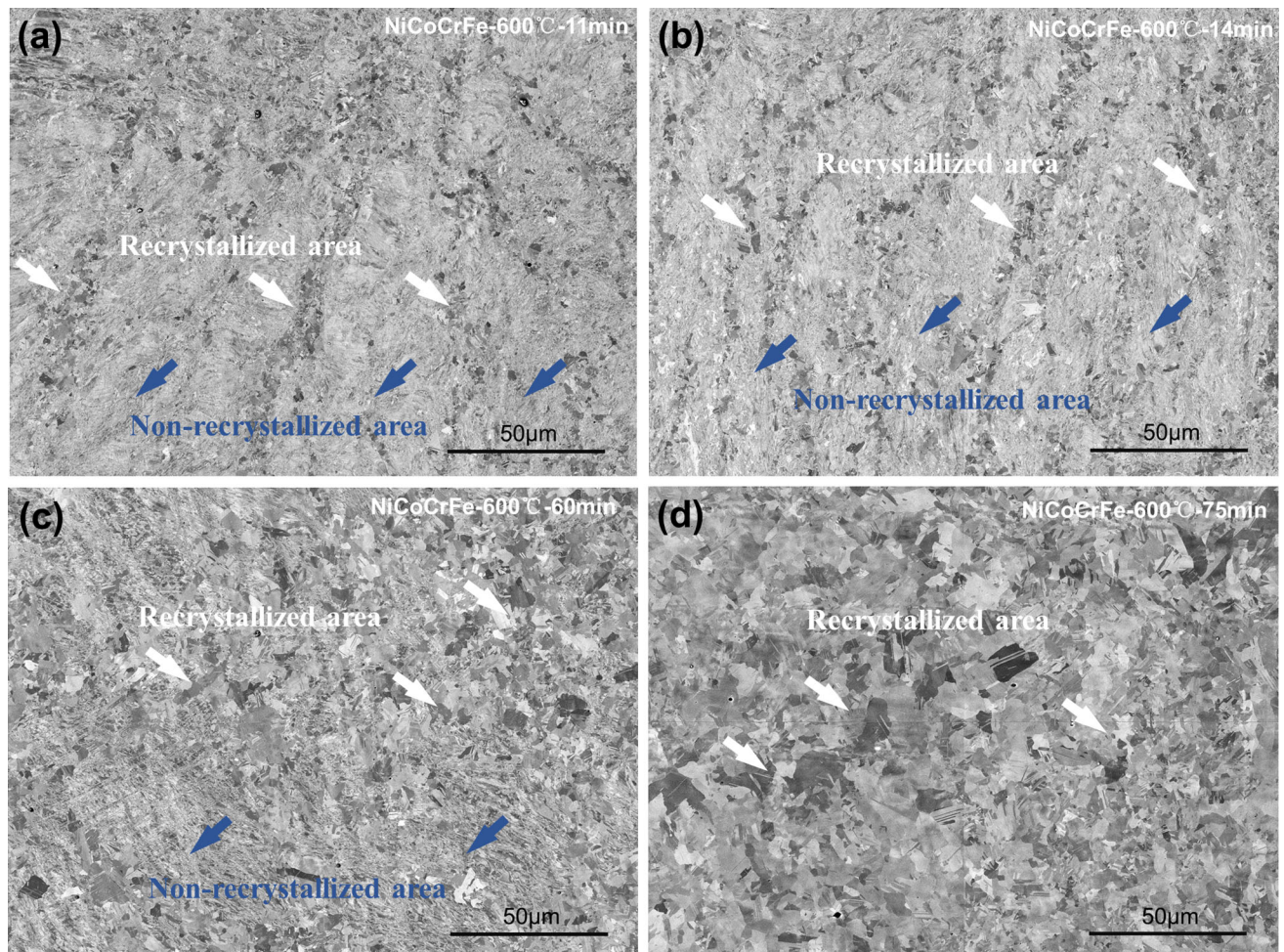


Fig. 2—Partially recrystallized microstructures of NiCoCrFe under 600 °C. (a) 11 min, (b) 14 min, (c) 60 min, and (d) 75 min.

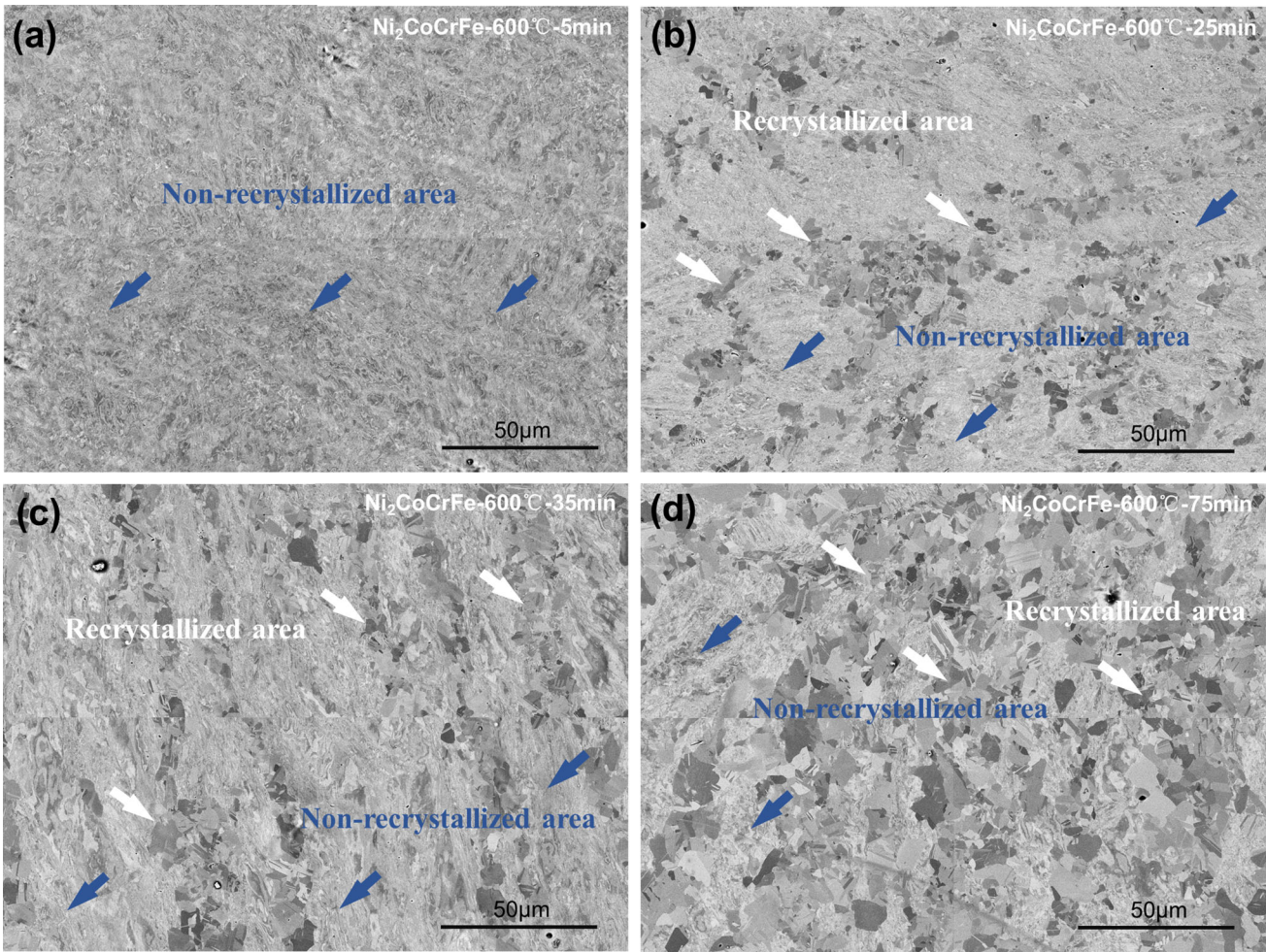


Fig. 3—Partially recrystallized microstructures of Ni_2CoCrFe under 600 °C. (a) 5 min, (b) 25 min, (c) 35 min, and (d) 75 min.

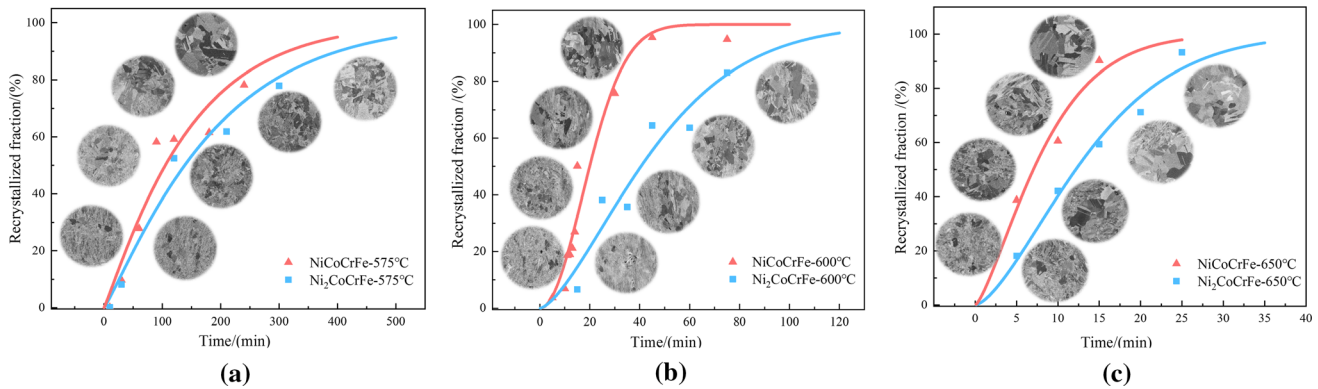


Fig. 4—Recrystallized fraction of NiCoCrFe and Ni_2CoCrFe vs. time under different temperatures. (a) 575 °C, (b) 600 °C, and (c) 650 °C.

recrystallization kinetics even though the compositions of the two HEAs are highly similar and undergo the same thermal-mechanical processing. For example, according to Figure 4(b), at 600 °C the 50 pct recrystallized fraction need ~ 20 minutes for NiCoCrFe , while more than 40 minutes is required for Ni_2CoCrFe . A similar trend in recrystallization kinetics of the two HEAs is also observed at 575 °C and 650 °C in

Figures 4(a) and (c). All kinetics curves show that NiCoCrFe owns a faster rate of recrystallization than Ni_2CoCrFe .

Here the JMAK model is adapted to quantitatively understand the recrystallization behaviors of the studied HEAs^[22]:

$$X = 1 - \exp(-Bt^n), \quad [1]$$

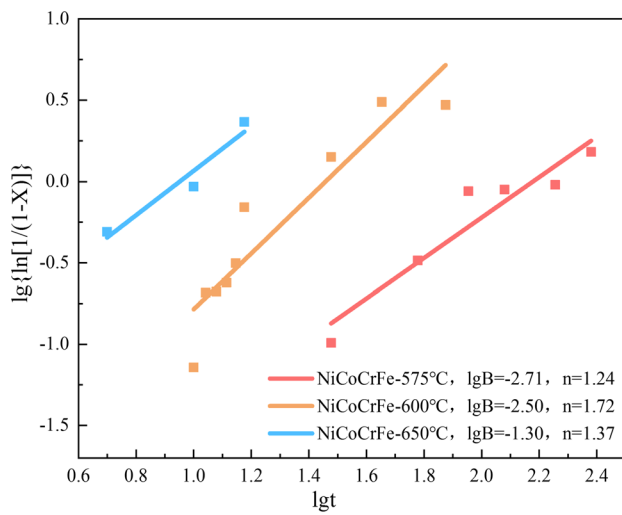
where X represents the recrystallized fraction of alloys (pct), t is the annealing time at the fixed temperature, B is a constant, and n is the Avrami exponent related with nucleation and growth pattern of the recrystallization. From the slopes of the Avrami plots, *i.e.*, $\lg\{\ln[1/(1-X)]\}$ vs. $\lg[\ln t]$ in Figures 5(a) and (b), the values of n can be calculated, whose values of NiCoCrFe and Ni₂CoCrFe locate in 1.24 to 1.72 and 1.24 to 1.83, respectively. According to fitted B and n , Figures 5(c) and (d) show the recrystallized fractions of both NiCoCrFe and Ni₂CoCrFe, from which it is obvious to find that both single-phase HEAs exhibit sigmoidal forms and short incubation periods of ~ 2 minutes at the investigated temperatures. After the incubation period, the recrystallization rate gradually increases up to 50 pct recrystallized fraction (midpoint), after which rate would decrease and stop at almost fully recrystallized fraction (~ 95 pct). According to the traditional definition of the recrystallization

temperature (at which the material has 50 pct recrystallized fraction in 1 hour heating treatment),^[22] recrystallization temperatures of 70 pct cold-rolled NiCoCrFe and Ni₂CoCrFe are around 600 °C.

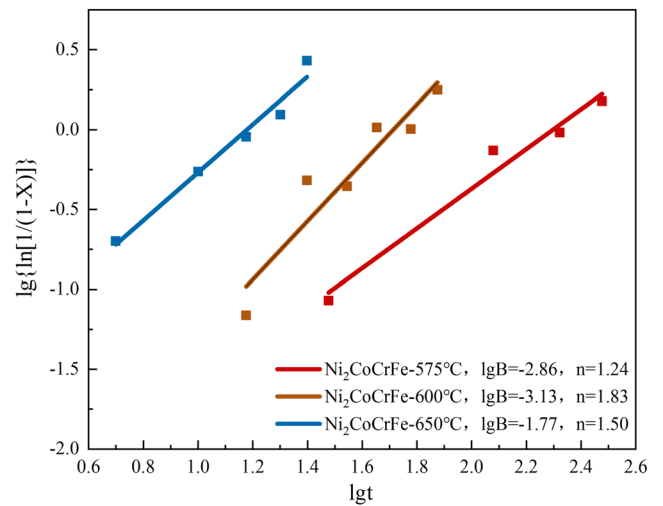
By comparing the two HEAs' recrystallization behaviors, it is surprising that the recrystallization rate of NiCoCrFe is faster than that of Ni₂CoCrFe under the same deformation and annealing conditions, which means a higher stored energy in NiCoCrFe. To understand the difference between the recrystallization kinetics of the two HEAs, the activation energies of recrystallization are analyzed using Arrhenius equation^[22]:

$$\frac{1}{t} = A \exp\left(-\frac{Q}{RT}\right), \quad [2]$$

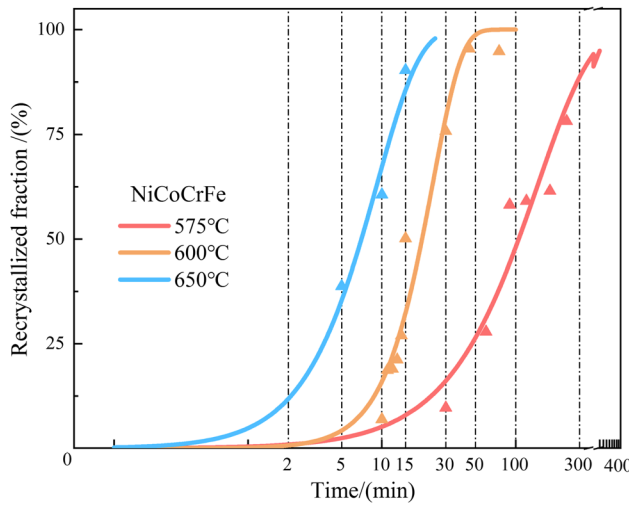
where t is the time of reaching the specific recrystallized fraction (50 pct was adopted here, $t_{0.5}$), R and T are the universal gas constant and annealing temperature,



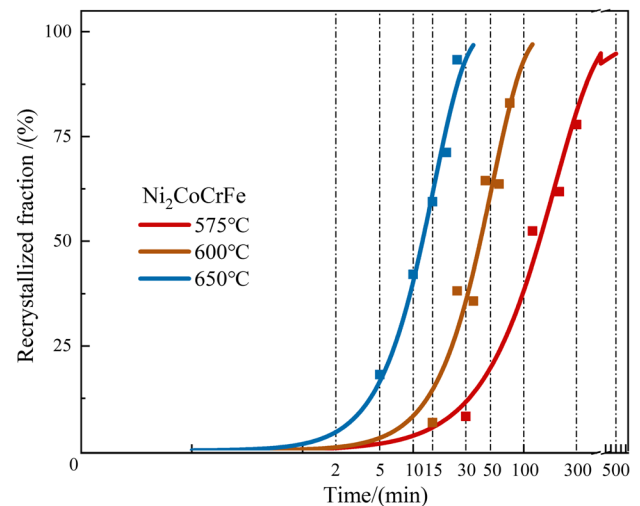
(a)



(b)



(c)



(d)

Fig. 5—Recrystallization kinetics of NiCoCrFe and Ni₂CoCrFe under cold-rolled 70 pct. (a, b) JMAK plots, and (c, d) recrystallized fraction vs. time plots.

respectively, A is the pre-exponential factor, and Q is the activation energy of recrystallization ($\text{kJ}\cdot\text{mol}^{-1}$), which can be extracted from the slopes of the curves in Figure 6: 234 and 221 $\text{kJ}\cdot\text{mol}^{-1}$ for NiCoCrFe and Ni₂CoCrFe, respectively.

In the classical theory,^[22] there are four main factors affecting the recrystallization kinetic, (a) initial grain size; (b) degree of deformation; (c) temperature of annealing; and (d) compositions of alloys, among which the prior three factors can be easily excluded since that (a) two alloys owned the same initial grain size of ~ 1 mm (Figure 7); (b) deformation degree had been strictly controlled around ~ 70 pct; (c) two alloys were under the same temperature and annealing circumstances.

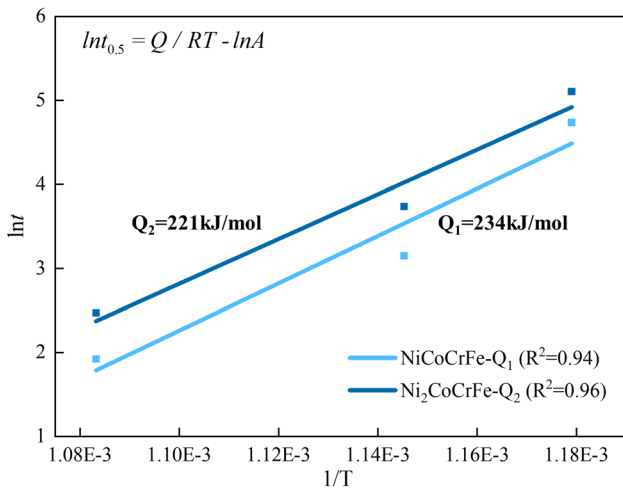


Fig. 6—Recrystallization activation energy of NiCoCrFe (Q1) and Ni₂CoCrFe (Q2) under 70 pct cold-rolled deformation.

Thus, it is rational to consider the composition factor that affects recrystallization kinetic. Traditionally, composition variation of alloys will mainly affect its properties: (1) melting point; (2) diffusivity; (3) stacking fault energy.

(1) Melting point, the heating temperature of 873 K ($600\text{ }^\circ\text{C}$) is referred to as the $0.522T_m$ for NiCoCrFe (melting point is around $1400\text{ }^\circ\text{C}$) and $0.513T_m$ for Ni₂CoCrFe (melting point of is around $1426\text{ }^\circ\text{C}$). Melting points of two alloys were calculated here by JMatPro software according to the Nickel-based Superalloy database in Figure 8 with a small difference of $26\text{ }^\circ\text{C}$. After transforming the Centigrade to Kelvin temperature, the heating temperature of 873 K ($600\text{ }^\circ\text{C}$) is referred to as the $0.522T_m$ for NiCoCrFe and $0.513T_m$ for Ni₂CoCrFe. Essentially, shear modulus correlated with melting points determines the value of stored energy and higher melting point means higher stored energy.^[22] However, interestingly, NiCoCrFe owns a higher stored energy but lower melting point than Ni₂CoCrFe and the melting point difference cannot explain such phenomenon.

(2) Diffusivity, activation energies for bulk diffusion of each element in the NiCoCrFe HEA sample are listed in Table I where Cr has the highest activation energy (323 kJ mol^{-1}) and Co has the lowest one (240 kJ mol^{-1}). Interestingly, the Q_{RX} extracted from the slope of the curve in Figure 6 amounts to 234 kJ mol^{-1} for NiCoCrFe, which are slightly less than the activation energy of bulk diffusion of Co (240 kJ mol^{-1}). With the increase of Ni content, corresponding values for Ni₂CoCrFe has not been provided. According to Vaidya's report,^[31] configuration of the constituents has a huge impact on the atomic diffusion and activation energy. In this regard, the average enthalpy of mixing for all individual components in the NiCoCrFe and Ni₂CoCrFe have been calculated from the following expression.^[31] Here, mixing enthalpy of binary pairs of elements of the multicomponent alloys are listed in Table II. Ideally, Ni₂CoCrFe is viewed as the

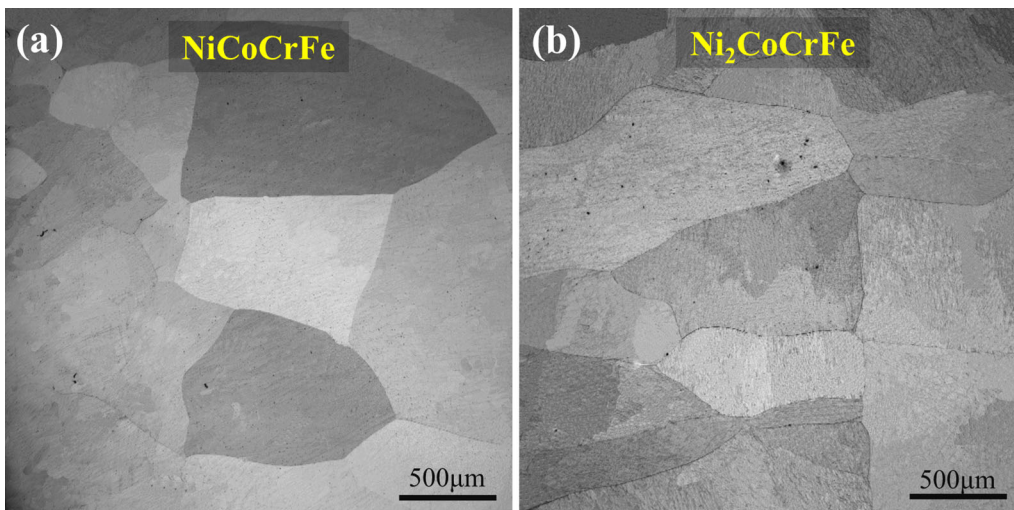


Fig. 7—BSE images of homogenized microstructures at $1200\text{ }^\circ\text{C}$ for 2 h. (a) NiCoCrFe, and (b) Ni₂CoCrFe.

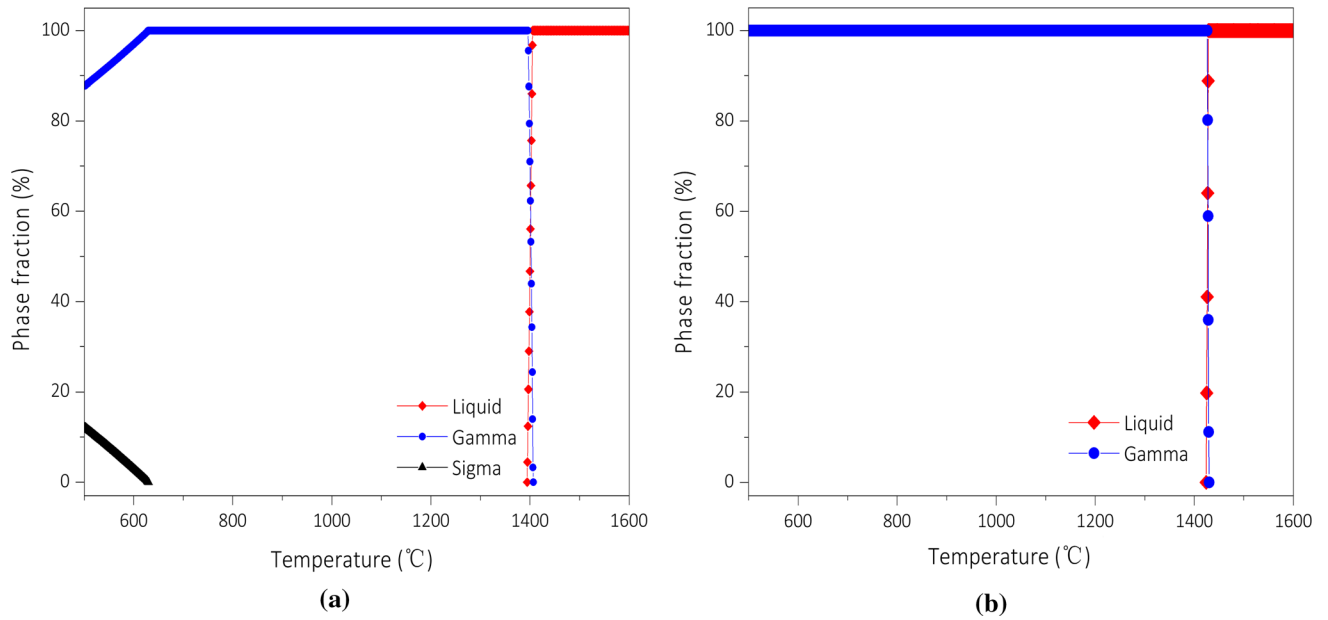


Fig. 8—Calculated phase diagrams of two alloys based on TTNi8 database. (a) NiCoCrFe and (b) Ni₂CoCrFe.

Table I. Activation Energies (kJ mol⁻¹) for Bulk Diffusion of Each Constituent Elements in NiCoCrFe^[28]

	Ni	Co	Cr	Fe
NiCoCrFe	253	240	323	303

equiatomic alloy which each element's mixing enthalpy is the same as NiCoCrFe.

$$\Delta H_{\text{avg}}^i = \frac{\sum_{j=1}^n \Delta H_{\text{mix}(ij)}}{n} \quad [3]$$

$\Delta H_{\text{mix}(ij)}$ is the binary mixing enthalpy of *i*th and *j*th element that was listed in Table III with the consideration of each element volume fraction.^[31] A more negative value of $\Delta H_{\text{avg}}^{\text{all}}$ in Ni₂CoCrFe (− 2.6) than NiCoCrFe (− 2.5) suggests a relatively strong binding of composed elements and hence an increased activation barrier for diffusion in Ni₂CoCrFe. However, the extrapolated recrystallization activation energies show the reverse result compared with the analyzed diffusion activation, implying bulk diffusion cannot control the recrystallization process in Ni–Co–Cr–Fe alloys which means the effect of diffusivity can also be excluded.

(3) **Stacking fault energy**, related studies have shown that the lower content of Ni causes a lower SFE in Ni–Co–Cr–Fe system,^[33–35] it is, therefore, reasonable to assume that the deformed state, which is significantly influenced by SFE, might be responsible for the difference in recrystallization kinetics of two HEAs. As shown in Figures 9(a) and (b), it is also obvious that two alloys exhibit different deformation microstructures. The

deformed NiCoCrFe shows many fringes with lighter contrast, which are hardly observed in deformed Ni₂CoCrFe. This difference in deformed microstructures between the two HEAs is confirmed by high-magnification BSE images in Figures 9(c) and (d).

To further understand these deformed microstructures, high-resolution EBSD and TEM analysis are carried out. Figures 10(a) and (c) respectively show the inverse pole figure (IPF) images of deformed NiCoCrFe and Ni₂CoCrFe, from which deformation twins (60 deg misorientation regions) are found in NiCoCrFe. As a contrast, there are only small misorientation changes in Ni₂CoCrFe across the profile line in Figures 10(b) and (d). The unindexed areas in Figure 10(c) are caused by the highly localized deformation in the slip bands and beyond the resolution limit required for reliable EBSD indexing.

These characters of the two HEAs are also confirmed by TEM. Both bright field (BF) and dark field (DF) graphs of the same area are obtained with selected area diffraction pattern (SAD) (Figure 11(a)), confirming the existence of typical deformation twins. However, there are only dislocation cells detected in BF with single set of diffraction pattern in Ni₂CoCrFe (Figure 11(b)). The different deformation mechanisms also result in distinct strain hardening behaviors. As shown in Figure 12, tensile stress of initial homogenized microstructure of NiCoCrFe is always higher than Ni₂CoCrFe. The different deformation mechanisms of the two HEAs are fully understandable since the decrease of Ni content can decrease the SFE and thus promote deformation twinning.^[34,38] Therefore, in the following, our discussion will focus on the effect of deformation twins on the recrystallization kinetics of HEAs.

On the one hand, it has been found that the deformation twins will hinder the dislocation movement and thus improve the stored energy of driving the

Table II. Mixing Enthalpy of Binary Pairs of Elements of the Multicomponent Alloys^[28]

Binary System	$\Delta H_{\text{mix}}(\text{kJmol}^{-1})$	Binary System	$\Delta H_{\text{mix}}(\text{kJmol}^{-1})$
Ni-Co	0	Co-Cr	- 4
Ni-Fe	- 2	Co-Fe	- 1
Ni-Cr	- 7	Cr-Fe	- 1

Table III. Average Enthalpies of Mixing (ΔH_{avg}^i) for All Constituents in NiCoCrFe and Ni₂CoCrFe With the Consideration of Element Volume Fraction

	Ni	Co	Cr	Fe	$\Delta H_{\text{avg}}^{\text{all}}$
NiCoCrFe	- 3 * 0.25	- 1.7 * 0.25	- 4 * 0.25	- 1.3 * 0.25	- 2.5
Ni ₂ CoCrFe	- 3 * 0.4	- 1.7 * 0.2	- 4 * 0.2	- 1.3 * 0.2	- 2.6

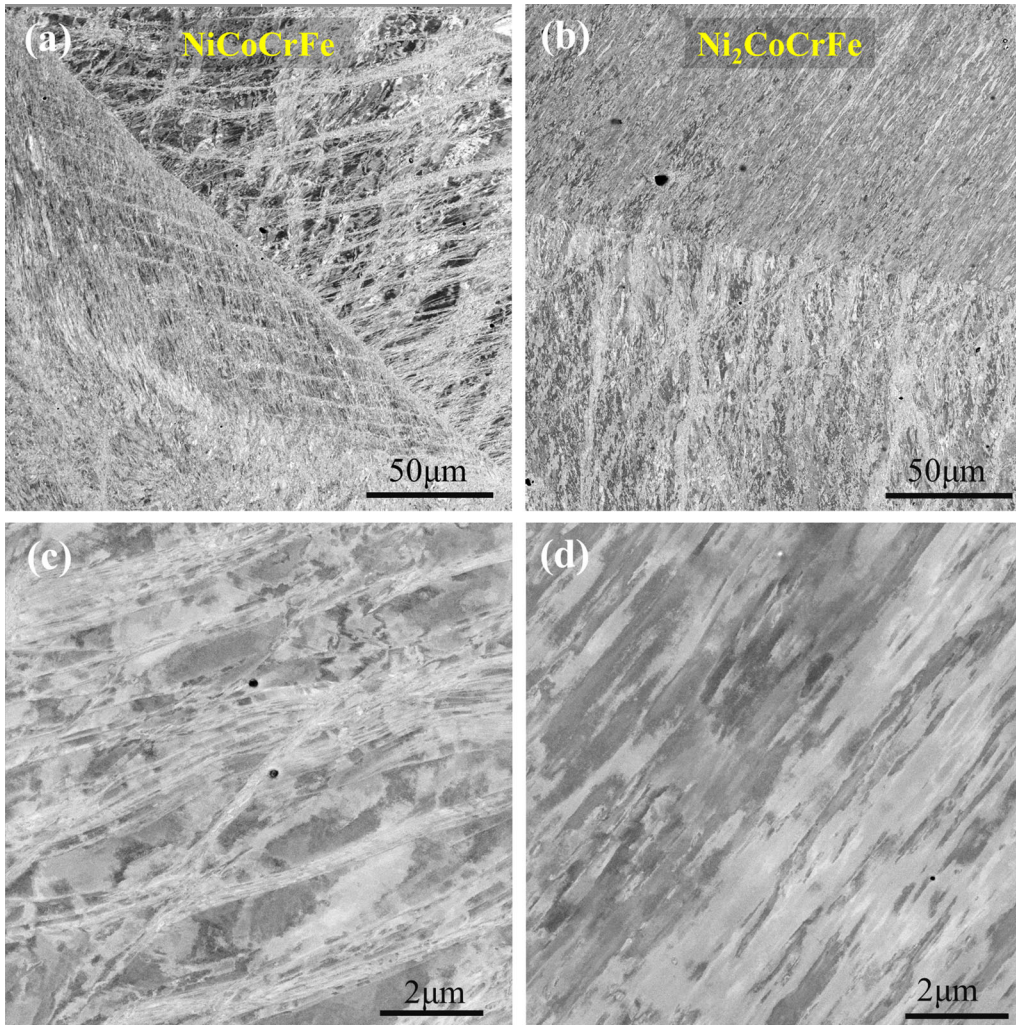


Fig. 9—BSE images of deformed microstructures after cold-rolled 70 pct. (a, c) NiCoCrFe, and (b, d) Ni₂CoCrFe.

recrystallizations.^[39–41] According to Bailey–Hirsch relationship,^[42] $\sigma = \sigma_y + MG\alpha b\sqrt{\rho}$ where the strain hardening ability is proportional to the square root of dislocation density, so it is reasonable to argue that a higher strain hardening may correspond to a higher

dislocation density. As shown in Figure 12, the homogenized NiCoCrFe ($\sigma_y \sim 188$ MPa, $\sigma_{\text{UTS}} \sim 479$ MPa) shows a similar yield strength but higher ultimate stress during deformation compared with Ni₂CoCrFe ($\sigma_y \sim 174$ MPa, $\sigma_{\text{UTS}} \sim 429$ MPa). Therefore, there is a higher

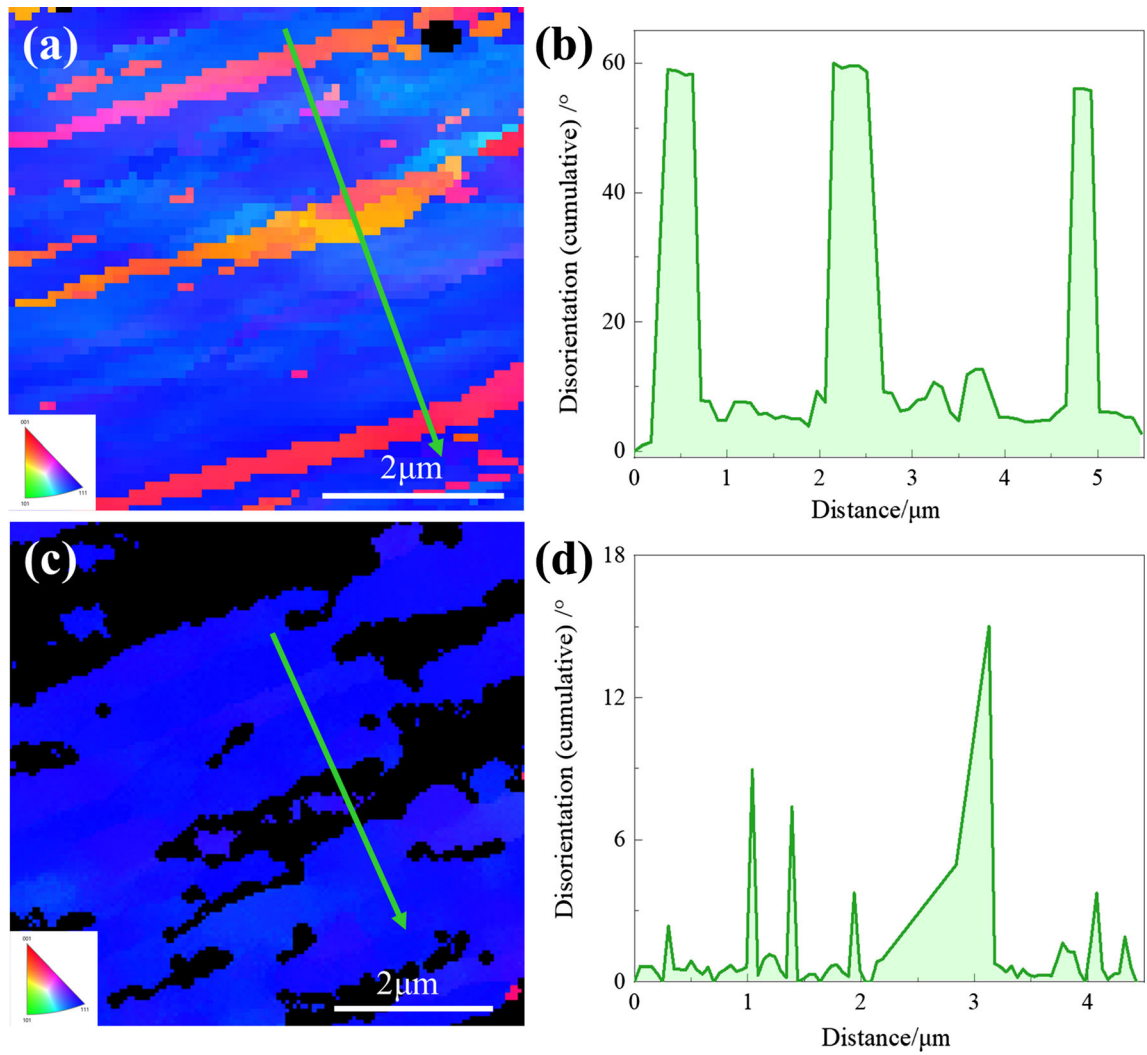


Fig. 10—EBSD images of deformed microstructures of NiCoCrFe and Ni₂CoCrFe cold-rolled ~ 70 pct. (a) IPF image of NiCoCrFe, (b) cumulative disorientation image of NiCoCrFe, (c) IPF image of Ni₂CoCrFe, and (d) cumulative disorientation image of Ni₂CoCrFe.

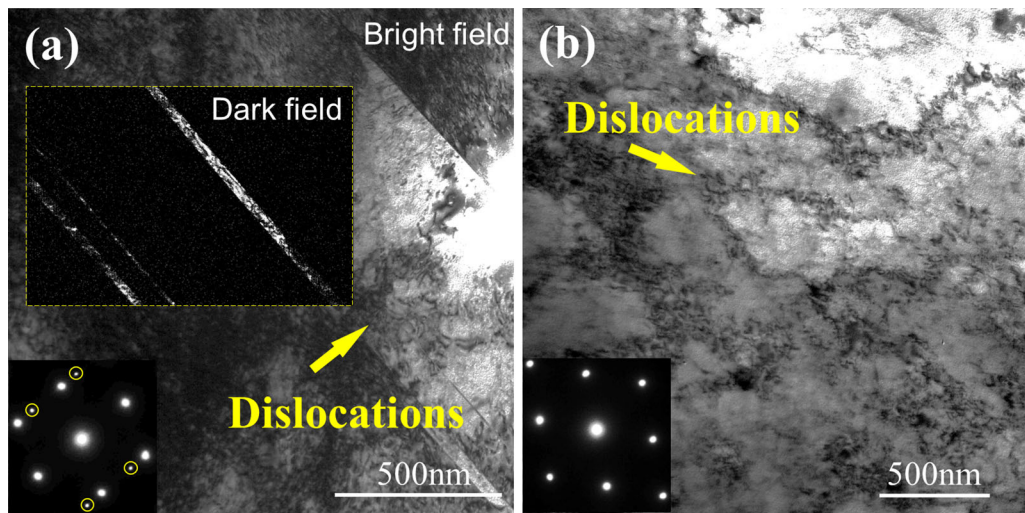


Fig. 11—TEM images of deformed microstructures of NiCoCrFe and Ni₂CoCrFe under cold-rolled 70 pct. (a) Bright field image of NiCoCrFe, the insets are the dark field image and the SAD corresponding to the same area. (b) Bright field image of Ni₂CoCrFe, the inset is the corresponding SAD.

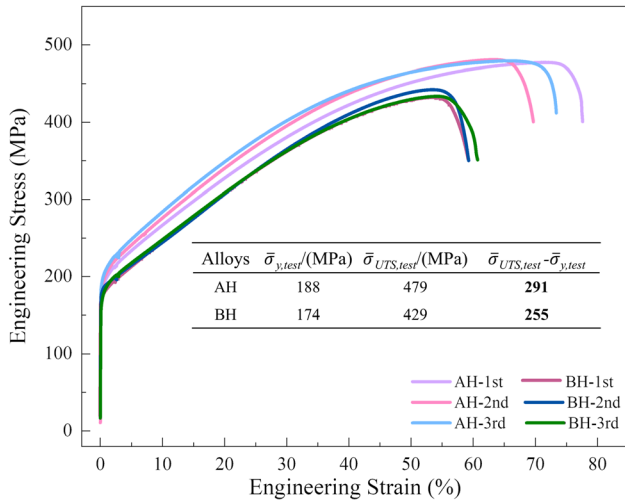


Fig. 12—Multi-tensile tests of the strength of NiCoCrFe and Ni₂CoCrFe under homogenized state.

dislocation density of the homogenized NiCoCrFe, which is induced by its characteristic deformation twins compared with the homogenized Ni₂CoCrFe.

On the other hand, deformation twins can also significantly affect microstructural inhomogeneity,^[43,44] which will act as the preferred nucleation sites of recrystallization. For instance, it has been found in α -titanium^[43] that twin boundaries and twinning-induced crystallographic lattice reorientation can improve the microstructural inhomogeneity, leading to a promoted static recrystallization process. In addition, more nucleation sites were also found in shear bands, grain boundaries and triple junctions of the Fe–Mn–C alloys,^[44] which were all inhomogeneities with localized orientation gradients. Similarly, in the present study, the deformation twins can also increase the heterogeneity of microstructure and act as the preferential nucleation sites for recrystallization.

Figure 13 shows the partially recrystallized microstructure of NiCoCrFe annealing for 53 minutes and Ni₂CoCrFe annealing for 61 minutes both under 600 °C. The nucleation patterns can be deduced from these characteristic partially recrystallized areas. As Figures 13(a) and (d) demonstrated, both two alloys nucleate at grain boundaries because grain boundary owns quantities of defects and high stored energy. The curve divides the recrystallized area and non-recrystallized area. In Figures 13(b) and (c), the distinct microstructures show different intragranular nucleation methods of two alloys. Figure 13(b) presents the intersection recrystallization areas in which the straight lines show the nucleation of twins and the curves show the nucleation of slip bands. Because of the existence of deformation twins, there are more potential nucleation sites in NiCoCrFe. In Ni₂CoCrFe, only slip bands nucleation area exists which is circled by curves. Other characteristic nucleation areas under higher magnification in Figures 13(c) and (d) also prove the existence of nucleation methods of deformation twins and slip bands in NiCoCrFe, while only slip bands nucleation in

Ni₂CoCrFe. These recrystallization nucleation modes are also supported by Avrami exponent. In Figure 5, Avrami exponent of NiCoCrFe varies between 1.24 and 1.72, and that of Ni₂CoCrFe varies between 1.24 and 1.83. These values indicate that the investigated HEAs do not follow the traditional site-saturated nucleation or random nucleation mechanisms, for which the Avrami exponents separately equal to 3 or 4.^[43,45] Such deviation of n from the classic values should be due to the heterogeneous recrystallization nucleation in Figure 13.^[45] Through the comparison of nucleation methods for two alloys, it indicates that more potential nucleation sites provided by twins cause a higher recrystallization rate and lead to faster recrystallization kinetics for NiCoCrFe consequently.

As a summary of former discussion, the role of deformation twins playing in the faster kinetics of recrystallization of NiCoCrFe can be concluded from two aspects. (1) Deformation twins result in higher stored energy by enhancing strain hardening capacity. (2) Deformation twins provide more potential nucleation sites for recrystallization.

IV. CONCLUSION

In the present work, the recrystallization kinetics of single-phase Ni–Co–Cr–Fe HEAs with different SFE were investigated. The major motivations of the current study were the lack of the quantified recrystallization kinetics as well as the unclarified mechanism of SFE effect the on recrystallization of HEAs. With the aid of SEM, EBSD, and TEM, we demonstrated that the increased stacking fault energy in Ni–Co–Cr–Fe-based single-phase HEAs can slow the recrystallization kinetics. Related deformation behaviors of two alloys had been studied and the recrystallization mechanism were discussed. The following conclusions can be made:

- Recrystallization kinetics curves of the single-phase Ni–Co–Cr–Fe HEAs show favorable coincidences with the JMAK model. The Avrami exponent of NiCoCrFe varies between 1.24 and 1.72, and that of Ni₂CoCrFe varies between 1.24 and 1.83.
- Under 70 pct cold-rolled deformation and 600 °C annealing temperature, NiCoCrFe shows higher recrystallization kinetics compared with Ni₂CoCrFe, though two HEAs have almost identical activation energies of 234 and 221 kJ·mol⁻¹ based on the Arrhenius equation.
- Profound deformation twins are found in NiCoCrFe while hardly detected in Ni₂CoCrFe by EBSD boundary disorientation analysis and the selected area diffraction pattern in TEM.
- Deformation twins result in higher local stored strain energy by enhancing strain hardening capacity and providing more potential nucleation sites, accelerating the recrystallization rate of NiCoCrFe. Based on these findings, the kinetics of recrystallization of HEAs can be controlled by adjusting the SFE of HEAs.

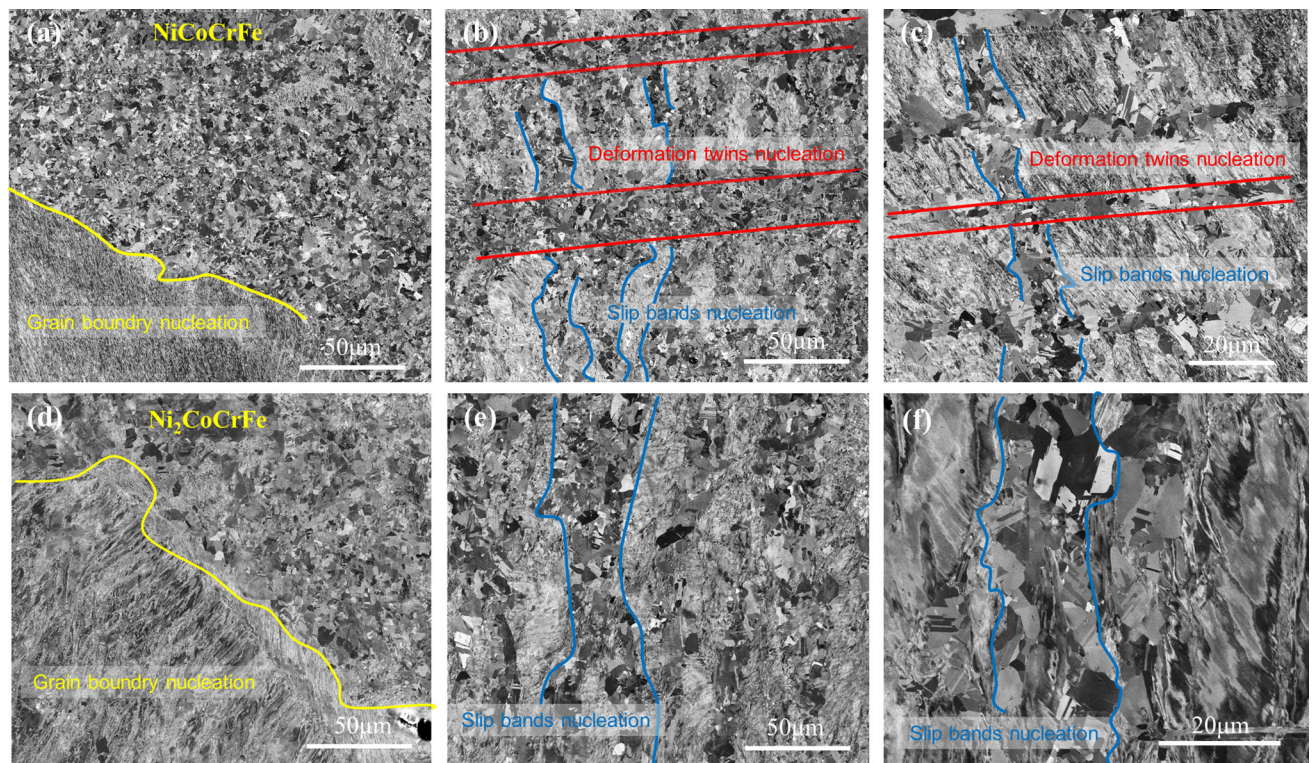


Fig. 13—BSE images of partially recrystallized microstructures of NiCoCrFe at 600 °C, 53 min and Ni₂CoCrFe at 600 °C, 61 min. (a) Grain boundary nucleation of NiCoCrFe, (b, c) intragranular nucleation of NiCoCrFe, (d) grain boundary nucleation of Ni₂CoCrFe, and (e, f) intragranular nucleation of Ni₂CoCrFe.

ACKNOWLEDGMENTS

The authors are grateful for the financial support from the National Key R&D Program of China (No. 2018YFB1106003), the National Natural Science foundation of China (Nos. 51771149, 52001266, and 51901119), Natural Science Foundation of Shaanxi Province in China (No. 2020JQ-720) and the Research Fund of the State Key Laboratory of Solidification Processing (NPU), China (Grant No. 2020-TS-06). Z. S. Yang is grateful to Y. Li for correcting of grammar and polishing the final manuscript.

CONFLICT OF INTEREST

On behalf of all authors, the corresponding author states that there is no conflict of interest.

SUPPLEMENTARY INFORMATION

The online version contains supplementary material available at <https://doi.org/10.1007/s11661-021-06341-2>.

REFERENCES

1. S. Wei, S.J. Kim, J. Kang, Y. Zhang, Y. Zhang, T. Furuwara, E.S. Park, and C.C. Tasan: *Nat. Mater.*, 2020, vol. 19, pp. 1175–81.
2. E.P. George, W.A. Curtin, and C.C. Tasan: *Acta Mater.*, 2019, vol. 188, pp. 435–74.
3. X. Wu, M. Yang, F. Yuan, G. Wu, Y. Wei, X. Huang, and Y. Zhu: *Proc. Natl Acad. Sci. USA*, 2015, vol. 112, pp. 14501–05.
4. X. Wu and Y. Zhu: *Mater. Res. Lett.*, 2017, vol. 5, pp. 527–32.
5. Y. Zhu, K. Ameyama, P.M. Anderson, I.J. Beyerlein, H. Gao, H.S. Kim, E. Lavernia, S. Mathaudhu, H. Mughrabi, R.O. Ritchie, N. Tsuji, X. Zhang, and X. Wu: *Mater. Res. Lett.*, 2021, vol. 9, pp. 1–31.
6. J.W. Yeh, S.K. Chen, S.J. Lin, J.Y. Gan, T.S. Chin, T.T. Shun, C.H. Tsau, and S.Y. Chang: *Adv. Eng. Mater.*, 2004, vol. 6, pp. 299–303.
7. Z. Li, S. Zhao, R.O. Ritchie, and M.A. Meyers: *Prog. Mater. Sci.*, 2019, vol. 102, pp. 296–345.
8. X.H. Du, W.P. Li, H.T. Chang, T. Yang, G.S. Duan, B.L. Wu, J.C. Huang, F.R. Chen, C.T. Liu, W.S. Chuang, Y. Lu, M.L. Sui, and E.W. Huang: *Nat. Commun.*, 2020, vol. 11, pp. 1–7.
9. C.E. Slone, J. Miao, E.P. George, and M.J. Mills: *Acta Mater.*, 2019, vol. 165, pp. 496–507.
10. M. Yang, D. Yan, F. Yuan, P. Jiang, E. Ma, and X. Wu: *Proc. Natl Acad. Sci. USA*, 2018, vol. 115, pp. 7224–29.
11. P. Shi, W. Ren, T. Zheng, Z. Ren, X. Hou, J. Peng, P. Hu, Y. Gao, Y. Zhong, and P.K. Liaw: *Nat. Commun.*, 2019, vol. 10, pp. 1–8.
12. Y. Lu, Y. Dong, H. Jiang, Z. Wang, Z. Cao, S. Guo, T. Wang, T. Li, and P.K. Liaw: *Scripta Mater.*, 2020, vol. 187, pp. 202–09.
13. Q. Wu, Z. Wang, X. Hu, T. Zheng, Z. Yang, F. He, J. Li, and J. Wang: *Acta Mater.*, 2020, vol. 182, pp. 278–86.
14. Y.L. Zhao, T. Yang, Y. Tong, J. Wang, J.H. Luan, Z.B. Jiao, D. Chen, Y. Yang, A. Hu, C.T. Liu, and J.J. Kai: *Acta Mater.*, 2017, vol. 138, pp. 72–82.

15. F. He, D. Chen, B. Han, Q. Wu, Z. Wang, S. Wei, D. Wei, J. Wang, C.T. Liu, and J. Jung Kai: *Acta Mater.*, 2019, vol. 167, pp. 275–86.
16. P. Sathiyamoorthi and H. Seop Kim: *Prog. Mater. Sci.*, 2020, vol. 115, pp. 100709–84.
17. V. Shivam, J. Basu, R. Manna, and N.K. Mukhopadhyay: *Metall. Mater. Trans. A*, 2021, <https://doi.org/10.1007/s11661-021-06188-7>.
18. J.W. Bae, J. Moon, M.J. Jang, D. Yim, D. Kim, S. Lee, and H.S. Kim: *Mater. Sci. Eng. A*, 2017, vol. 703, pp. 324–30.
19. Z. Fu, B.E. Macdonald, Z. Li, Z. Jiang, W. Chen, Y. Zhou, and E.J. Lavernia: *Mater. Res. Lett.*, 2018, vol. 6, pp. 634–40.
20. E. Ma and X. Wu: *Nat. Commun.*, 2019, vol. 10, pp. 1–10.
21. J. He: *Scripta Mater.*, 2020, vol. 187, pp. 1–3.
22. A. Rollett, F. Humphreys, G.S. Rohrer, and M. Hatherly: *Recrystallization and Related Annealing Phenomena*, 3rd ed., Elsevier, Amsterdam, 2004.
23. S.W. Wu, G. Wang, Y.D. Jia, J. Yi, Q.J. Zhai, C.T. Liu, B.A. Sun, H.J. Chu, J. Shen, P.K. Liaw, and T.Y. Zhang: *Acta Mater.*, 2019, vol. 165, pp. 444–58.
24. J. Kang, N. Park, J.K. Kim, and J.H. Park: *Mater. Sci. Eng. A*, 2021, vol. 814, p. 141249.
25. M. Annasamy, N. Haghdadi, A. Taylor, P. Hodgson, and D. Fabijanic: *Mater. Sci. Eng. A*, 2019, vol. 754, pp. 282–94.
26. M. Annasamy, N. Haghdadi, A. Taylor, P. Hodgson, and D. Fabijanic: *Mater. Sci. Eng. A*, 2019, vol. 745, pp. 90–106.
27. X. Liang, Q. Wu, H. Li, R.X. Wang, L. Kang, B. Liu, and L. Wang: *J. Alloys Compd.*, 2021, vol. 862, p. 158602.
28. M. Vaidya, K.G. Pradeep, B.S. Murty, G. Wilde, and S.V. Divinski: *Acta Mater.*, 2018, vol. 146, pp. 211–24.
29. M. Vaidya, K.G. Pradeep, B.S. Murty, G. Wilde, and S.V. Divinski: *Sci. Rep.*, 2017, vol. 7, pp. 1–11.
30. K.Y. Tsai, M.H. Tsai, and J.W. Yeh: *Acta Mater.*, 2013, vol. 61, pp. 4887–97.
31. M.H. Mohammad Ebrahimi, A. Zarei-Hanzaki, H.R. Abedi, S.M. Vakili, and C.K. Soundararajan: *J. Alloys Compd.*, 2019, vol. 806, pp. 1550–63.
32. Z. Wu, H. Bei, F. Otto, G.M. Pharr, and E.P. George: *Intermetallics*, 2014, vol. 46, pp. 131–40.
33. S.F. Liu, Y. Wu, H.T. Wang, J.Y. He, J.B. Liu, C.X. Chen, X.J. Liu, H. Wang, and Z.P. Lu: *Intermetallics*, 2018, vol. 93, pp. 269–73.
34. A.J. Zaddach, C. Niu, C.C. Koch, and D.L. Irving: *JOM*, 2013, vol. 65, pp. 1780–89.
35. F. He, Z. Wang, B. Han, Q. Wu, D. Chen, J. Li, J. Wang, C.T. Liu, and J.J. Kai: *J. Alloys Compd.*, 2018, vol. 769, pp. 490–502.
36. J.P. Panda, P. Arya, K. Guruvadyathri, S. Ravikiran, and B.S. Murty: *Metall. Mater. Trans. A*, 1997, vol. 52, pp. 1679–88, <https://doi.org/10.1007/s11661-021-06162-3>.
37. Y. Liu, Y. Cao, Q. Mao, H. Zhou, Y. Zhao, W. Jiang, Y. Liu, J.T. Wang, Z. You, and Y. Zhu: *Acta Mater.*, 2020, vol. 189, pp. 129–44.
38. E.E.D.S. Asgari and R.D.D.S.R. Kalidindi: *Metall. Mater. Trans. A*, 1997, vol. 28, pp. 1781–82.
39. D. Guan, W.M. Rainforth, L. Ma, B. Wynne, and J. Gao: *Acta Mater.*, 2017, vol. 126, pp. 132–44.
40. I. Basu and T. Al-Samman: *Acta Mater.*, 2015, vol. 96, pp. 111–32.
41. X. Li, P. Yang, L.N. Wang, L. Meng, and F. Cui: *Mater. Sci. Eng. A*, 2009, vol. 517, pp. 160–69.
42. J.E. Bailey and P.B. Hirsch: *Philos. Mag. A*, 1960, vol. 5, pp. 485–97.
43. J.W. Won, T. Lee, S.G. Hong, Y. Lee, J.H. Lee, and C.S. Lee: *Met. Mater. Int.*, 2016, vol. 22, pp. 1041–48.
44. Y. Lü, D.A. Molodov, and G. Gottstein: *Acta Mater.*, 2011, vol. 59, pp. 3229–43.
45. M. Oyarzábal, A. Martínez-de-Guerenu, and I. Gutiérrez: *Mater. Sci. Eng. A*, 2008, vol. 485, pp. 200–09.

Publisher's Note Springer Nature remains neutral with regard to jurisdictional claims in published maps and institutional affiliations.